Dalton Transactions

ROYAL SOCIETY OF CHEMISTRY

PAPER

View Article Online
View Journal

Cite this: DOI: 10.1039/d5dt01698c

Two reduced phosphomolybdate-based metal–organic complexes modified by tunable bis-1*H*-benzimidazole ligands for enhanced photocatalytic Cr(VI) reduction

Feng-Cai Li, * Xi-Li Li, Yu-Zhe Pan, Cong-Li Gao and Qing-Xiang Yang

Received 18th July 2025,
Accepted 10th September 2025

DOI: 10.1039/d5dt01698c

rsc.li/dalton

The strategic development of polyoxometalate-based complexes for enhanced photocatalytic Cr(VI) reduction in wastewater remains a significant challenge in environmental remediation. In this work, two flexible bis-1*H*-benzimidazole ligand-functionalized reduced phosphomolybdate-based complexes with the formulas $(H_2bbbm)_3[Mn(H_2O)_2]\{Mn[P_4Mo_6^{V}O_{31}H_7]_2\}\cdot 8H_2O$ (**1**) and $(H_2bbbm)_3\{Ni[P_4Mo_6^{V}O_{31}H_8]_2\}\cdot 6H_2O$ (**2**) (bbbm = 1,1′-(1,4-butanediyl)bis-1*H*-benzimidazole) were hydrothermally prepared and comprehensively characterized by multiple analytical techniques. Single-crystal analysis reveals that compound **1** exhibits a 3D network structure constructed through hierarchical assembly: Mn^{2+}-bridged $\{Mn[P_4Mo_6O_{31}H_7]_2\}^{8-}$ dimers first form 1D inorganic chains, which are then interconnected by protonated $[H_2bbbm]^{2+}$ ions *via* supramolecular interactions to generate the final 3D architecture. However, compound **2** is revealed as a 3D supramolecular network, which is formed by classical 0D $\{Ni[P_4Mo_6^{V}O_{31}H_8]_2\}^{6-}$ dimeric clusters and protonated $[H_2bbbm]^{2+}$ ions. When employed as visible-light photocatalysts, compounds **1** and **2** manifested excellent photocatalytic performance in Cr(VI) reduction with removal rates of 99.25% for **1** and 98.09% for compound **2** after only 8 minutes, respectively. In addition, the reduction process followed pseudo-first-order kinetics with respect to Cr(VI) concentration, exhibiting outstanding *k* values of 0.623 min^{-1} for compound **1** and 0.511 min^{-1} for compound **2**, respectively. Notably, compound **1** demonstrates superior photocatalytic performance. Meanwhile, both compounds still displayed excellent capability for Cr(VI) reduction in real water samples, underscoring their significant potential for practical application. Mechanistic studies demonstrate that the $M\{P_4Mo_6\}_2$ clusters play a critical role in photocatalytic performance. The synergistic effect among polyoxometalate anions, bridging metal centers (M), and the flexible bis(1*H*-benzimidazole) ligand enhances photocatalytic activity by modulating the band gap of the photocatalysts. This study establishes a design strategy for high-performance visible-light photocatalysts by adjusting the structural composition of reduced phosphomolybdate systems, offering new solutions for environmental pollutant treatment.

Introduction

The treatment of wastewater containing numerous heavy metal ions has emerged as a pressing environmental challenge in recent years.[1,2] Among them, hexavalent chromium (Cr(VI)) ions, as a prevalent and highly toxic heavy metal pollutant, is ubiquitously detected in wastewater from electroplating, metallurgical, tanning, and related industries.[3] Owing to its high solubility, discharged Cr(VI) becomes readily bioavailable in aquatic systems, endangering human health and ecosystems through bio-accumulative pathways.[4,5] Consequently, the elimination of toxic Cr(VI) from aqueous environments is a crucial objective. Currently, conventional techniques including adsorption, chemical precipitation, and ion exchange have been widely employed for Cr(VI) removal, but they often suffer from notable drawbacks, including high operational costs, limited treatment efficiency, and the potential risk of secondary pollution from residual reagents or sludge by-products.[6,7] Among various remediation technologies, photocatalysis technology has been considered a highly effective and promising approach for Cr(VI) reduction.[8–10] While conventional semiconductor photocatalysts established the conceptual basis for Cr(VI) reduction, their widespread applications have been hindered by inherent material limitations including wide band gaps, and rapid charge recombination. Hence, the develop-

Key Laboratory of Surface & Interface Science and Technology, School of Materials and Chemical Engineering, Zhengzhou University of Light Industry, Zhengzhou, Henan Province, 450002, People's Republic of China. E-mail: lifengcai85@163.com; Tel: +86 15038286508

ment of high-performance photocatalysts constitutes the central challenge in achieving efficient Cr(VI) photoreduction.

Polyoxometalates (POMs), a class of well-defined inorganic polynuclear metal-oxo clusters, have garnered significant interest in materials chemistry owing to their fascinating structural architectures and broad application potential across diverse fields such as magnetic materials, organic catalysis, adsorption processes, electrochemistry, and photochemistry.[11–13] Among them, reduced sandwich-type phosphomolybdate $\{M^n[P_4Mo_6^VO_{31}H_X]_2\}^{(24-2x-n)-}$ (abbreviated $M\{P_4Mo_6\}_2$) clusters have attracted widespread interest.[14,15] This is because $M\{P_4Mo_6\}_2$ clusters not only exhibit distinctive features, such as abundant surface-exposed oxygen sites, high negative charge density, and exceptional redox activity, but they also resemble semiconductor metal oxides structurally and electronically.[16,17] In recent years, $M\{P_4Mo_6\}_2$-based metal–organic complexes (MOCs) have demonstrated remarkable multifunctionality, finding applications across diverse domains including organic catalysis, proton conduction, supercapacitors, electrochemistry, and photochemistry.[18–22] In general, the construction of high-performance $M\{P_4Mo_6\}_2$-based MOCs with innovative architectures can be systematically engineered through three key design dimensions as follows. First, the variation of the central metal M in $M\{P_4Mo_6\}_2$ clusters substantially affects their photocatalytic activity by tuning the electronic structure.[15,23] For instance, Han's group evidenced that the central metal ion M (M = Mn, Co) in $M\{P_4Mo_6\}_2$ clusters plays a decisive role in Cr(VI) photoreduction, where Mn-based complexes exhibited superior activity over Co-based analogues due to optimized electronic structure modulation.[24] Second, the oxygen-rich surfaces of the aforementioned $M\{P_4Mo_6\}_2$ units facilitate the construction of extended frameworks *via* coordination with different metal linkers.[25–27] Finally, the self-assembly behavior of $M\{P_4Mo_6\}_2$-derived MOCs is highly dependent on organic ligand selection. The structural arrangement of these clusters is strongly affected by the ligand's charge state, size, and conformational properties.[28–30] For example, Han's group established that the organic components with different degrees of conjugation can regulate the photocatalytic performance of $\{Zn[P_4Mo_6]_2\}$ cluster-based MOCs for hexavalent chromium reduction.[31] Among numerous N-containing ligands, bis(1*H*-benzimidazole) derivatives have attracted our interest due to their features as follows. First, multiple nitrogen atoms (N-donors from the imidazole rings) in the bis-benzimidazole structure can simultaneously coordinate to the metal centres, enabling the formation of stable chelates or bridging structures.[32] Second, the benzimidazole ring possesses a rigid aromatic structure, which endows it with stability in both acidic and alkaline environments, making it suitable for catalysis or materials synthesis across a broad pH range.[33] Third, the protonation-induced charge modulation of bis(1*H*-benzimidazole) derivatives enables stabilization of anionic metal complexes with improved solvation properties in aqueous solution.[34] Thus, the unique features of bis-1*H*-benzimidazole derivatives make them prime candidates for engineering $M\{P_4Mo_6\}_2$-derived MOCs with tuneable architectures and enhanced functional properties. To the best of our knowledge, no previous studies have reported the incorporation of bis(1*H*-benzimidazole) ligands into $M\{P_4Mo_6\}_2$-based MOCs.

Taking all of these features into account, two $M\{P_4Mo_6\}_2$-based MOCs with the formulas $(H_2bbbm)_3[Mn(H_2O)_2]\{Mn[P_4Mo_6O_{31}H_7]_2\}\cdot 8H_2O$ (**1**) and $(H_2bbbm)_3\{Ni[P_4Mo_6O_{31}H_8]_2\}\cdot 6H_2O$ (**2**) (bbbm = 1,1′-(1,4-butanediyl)bis-1*H*-benzimidazole) were hydrothermally prepared by introducing flexible bis-1*H*-benzimidazole ligands. Structural analyses proved that compounds **1** and **2** have different 3D supramolecular structures. For compound **1**, the $Mn\{P_4Mo_6\}_2$ clusters are bridged by Mn(II) ions to form 1D chains, which subsequently interact with protonated $[H_2bbbm]^{2+}$ ions through supramolecular interactions to generate a 3D framework. However, compound **2** displays a 3D supramolecular structure assembled through the interaction of protonated $[H_2bbbm]^{2+}$ ions and 0D $Ni\{P_4Mo_6\}_2$ clusters. Notably, both compounds constitute the first documented examples of $M\{P_4Mo_6\}_2$-based MOCs incorporating the bbbm ligand. When employing these MOCs as visible-light-driven photocatalysts, compounds **1** and **2** exhibited promising Cr(VI) reduction performance, with compound **1** achieving 99.25% removal efficiency and compound **2** reaching 98.09% removal efficiency after only 8 minutes of irradiation, respectively. In addition, photocatalytic evaluation demonstrates that compound **1** achieves significantly higher activity than compound **2**, likely due to the enhanced active site accessibility afforded by its one-dimensional chain-like architecture. The possible photocatalytic mechanisms were explored. This study offers a feasible approach to designing high-performance polyoxometalate (POM)-based MOCs for efficient photocatalytic Cr(VI) reduction under visible-light irradiation.

Experimental section

Chemicals and methods

All chemical reagents and solvents were obtained from commercial sources and employed without further treatment. The 1,1′-(1,4-butanediyl)bis-1*H*-benzimidazole (abbreviated to bbbm) ligand was prepared according to established literature procedures (Scheme 1 and Scheme S1).[35] Full experimental details regarding characterization techniques (PXRD, FTIR spectroscopy, elemental analysis, TGA, UV–vis spectroscopy, XPS) and electrochemical measurements and photocatalytic tests are provided in detail in the SI.

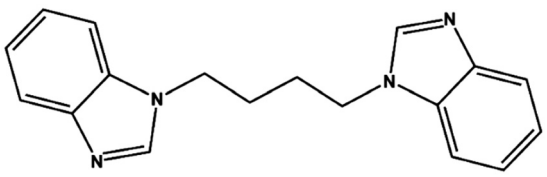

Scheme 1 1,1′-(1,4-Butanediyl)bis-1*H*-benzimidazole (abbreviated To bbbm) used in this paper.

X-ray crystallography

Single-crystal X-ray diffraction data of compounds **1** and **2** were acquired on a Bruker Smart CCD diffractometer equipped with Mo Kα radiation (λ = 0.71073 Å) at 293 K. The structures of compounds **1** and **2** were solved by the Olex2 software.[36] Crystal data and structure refinement for compounds **1** and **2** are listed in Table 1. Selected bond lengths and angles of compounds **1** and **2** are provided in Tables S1–S4 (SI). The final refined crystallographic data of compounds **1** and **2** have been deposited with the Cambridge Crystallographic Data Centre and assigned CCDC reference numbers 2449146 (**1**) and 2449148 (**2**), respectively.

Synthesis of $(H_2bbbm)_3[Mn(H_2O)_2]\{Mn[P_4Mo_6O_{31}H_7]_2\}\cdot 8H_2O$ (1)

In a 25 mL beaker, $MnCl_2\cdot 4H_2O$ (0.099 g, 0.5 mmol), $Na_2MoO_4\cdot 2H_2O$ (0.242 g, 1.0 mmol), and bbbm (0.058 g, 0.2 mmol) were sequentially added, followed by the addition of H_3PO_4 (85%, 0.5 mL, 7.5 mmol) and C_2H_5OH/H_2O (1 : 5, V/V, 6 mL). After stirring the mixture magnetically for 30 minutes at room temperature, the pH was carefully adjusted to 1.52 using 1 M NaOH solution. The resulting solution was then transferred to a 25 mL Teflon-lined stainless steel autoclave. The reaction mixture was heated at 160 °C for 96 h and followed by controlled cooling to ambient temperature at a rate of 5 °C h^{-1}.

Deep-red rhombohedral crystals of compound **1** were acquired and isolated (yield: 75% based on Mo). Elemental analysis for $C_{54}H_{94}Mn_2Mo_{12}N_{12}O_{72}P_8$ (%): C, 18.16; H, 2.65; N, 4.71. Found (%): C, 18.14; H, 2.63; N, 4.72. Selected IR spectroscopy (cm^{-1}): 3574(w), 3136(w), 3063(w), 2864(w), 1619(w), 1551(w), 1419(m), 1386(w), 1318(w), 1260(w), 1084(s), 1021(s), 963(s), 807(w), 749(s), 686(m), 612(m), 501(s).

Table 1 Crystal data and structure refinement for compounds **1** and **2**

Compound	**1**	**2**
Empirical formula	$C_{54}H_{94}Mn_2Mo_{12}N_{12}O_{72}P_8$	$C_{54}H_{88}Mo_{12}N_{12}NiO_{68}P_8$
Formula weight	3572.30	3451.08
Crystal system	Triclinic	Triclinic
Space group	$P\bar{1}$	$P\bar{1}$
a (Å)	14.345(2)	13.3340(17)
b (Å)	14.641(2)	14.8273(19)
c (Å)	15.037(2)	15.1027(19)
α (°)	65.575(2)	98.590(2)
β (°)	65.603(2)	110.121(2)
γ (°)	68.792(2)	105.761(2)
V (Å^3)	2548.4(6)	2599.0(6)
Z	1	1
D_c (g cm^{-3})	2.291	2.172
μ (mm^{-1})	1.903	1.804
F (000)	1712	1656
Reflections collected	60 660	63 042
Unique reflections	10 728	10 843
Parameters	719	706
R_{int}	0.0421	0.0349
GOF	1.143	1.115
R_1 [a] [$I > 2\sigma(I)$]	0.0497	0.0533
wR_2 [b] (all data)	0.1195	0.1576
CCDC	2449146	2449148

[a] $R_1 = \sum||F_o| - |F_c||/\sum|F_o|$. [b] $wR_2 = \sum[w(F_o^2 - F_c^2)^2]/\sum[w(F_o^2)^2]^{1/2}$.

Synthesis of $(H_2bbbm)_3\{Ni[P_4Mo_6O_{31}H_8]_2\}\cdot 6H_2O$ (2)

Compound **2** was assembled analogously to compound **1**, with the differences being that (a) $NiCl_2\cdot 6H_2O$ (0.119 g, 0.5 mmol) was used as the metal source instead of $MnCl_2\cdot 4H_2O$, and (b) the reaction mixture was carefully titrated to pH 1.46 prior to heating. Deep-red block crystals of **2** were obtained in 68% yield (based on Mo). Elemental analysis for $C_{54}H_{88}Mo_{12}N_{12}NiO_{68}P_8$ (%): C, 18.79; H, 2.57; N, 4.87. Found (%): C, 18.77; H, 2.54; N, 4.85. Selected IR (solid KBr pellet, cm^{-1}): 3569(w), 3131(w), 3058(w), 2922(w), 2859(w), 1624(w), 1546(w), 1444(m), 1376(w), 1318(w), 1260(w), 1089(s), 1041(s), 963(s), 744(s), 681(m), 603(m), 520(s).

Results and discussion

Synthesis discussion

Compounds **1** and **2** were hydrothermally obtained from reacting Na_2MoO_4, H_3PO_4, $MnCl_2\cdot 4H_2O$, $CoCl_2\cdot 6H_2O$, and bbbm ligand in a mixture of C_2H_5OH/H_2O solvent at 160 °C for 96 h. During the reaction process, the bbbm ligand acts as a reducing agent to reduce Mo^{VI} to Mo^{V}. To obtain high-purity single crystals, multiple parallel syntheses were performed under systematically varied conditions. First, the molar ratio of M^{2+} to bbbm ligand significantly influences the quality of the final products. At the metal-to-ligand ratio of 5 : 2, compounds **1** and **2** exhibited optimal purity. When the M^{2+}/bbbm ratio was increased from 3 : 2, 1 : 1, to 1 : 2, the product yield was significantly diminished under these conditions. Second, the influence of solution pH on crystal formation was systematically investigated, revealing a narrow optimal window (pH = 1.5–2.5) for obtaining diffraction-quality single crystals. Specifically, adjusting the pH to 1.52 favored the formation of compound **1**, which featured a 1D Mn-$\{Mn[P_4Mo_6]_2\}$ chain. When the pH was set to 1.46, compound **2** with 0D $\{Ni[P_4Mo_6]_2\}$ was generated. However, a mass of precipitates was obtained while the pH value was higher (pH > 3.0) or lower (pH < 1.5). Third, the N-containing bbbm ligand is an important factor. The bbbm ligand not only creates a reducing environment for the reaction system but also undergoes protonation to form counterions. These counterions balanced the negative charge of $M\{P_4Mo_6\}_2$ clusters. These results were consistent with the role of N-containing ligands used in the literature.[37] The bond valence sum analysis indicates that all molybdenum and phosphorus atoms are in the +5 oxidation states in compounds **1** and **2**. Meanwhile, the Mn and Ni centers maintain +2 oxidation states (Table S7).

Structural description

Single-crystal X-ray structural determination confirmed that compound **1** belongs to the triclinic crystal system with the $P\bar{1}$ space group (Table 1). The asymmetric unit of this system con-

sists of 1/2 $\{Mn[P_4Mo_6O_{31}H_7]_2\}^{8-}$ cluster, 1/2 $[Mn(H_2O)_2]^{2+}$ ions, 3/2 protonated $[H_2bbbm]^{2+}$ ions, and eight lattice water molecules (Fig. S1). X-ray crystallography reveals two types of crystallographically unique Mn sites (Mn1 and Mn2) in the structure. As shown in Fig. 1a and S2, the metal ion, as the central metal ion Mn1 of the $Mn\{P_4Mo_6\}_2$ unit, adopts a slightly distorted hexacoordinate octahedral geometry, bridging the $[P_4Mo_6O_{31}H_7]^{5-}$ clusters by six oxygen atoms to construct a sandwich-type $\{Mn[P_4Mo_6O_{31}H_7]_2\}^{8-}$ cluster. This structural feature is consistent with the $\{Mn[P_4Mo_6O_{31}H_7]_2\}^{8-}$ cluster reported in the literature.[27] The bond distances of the Mn1–O bonds vary between 2.213(4) Å and 2.217(4) Å with an average distance of 2.205 Å. The metal ion Mn2 also exhibits a six-coordinate environment, connected by four O atoms (O27, $O27^1$, O29, and $O29^1$) from $\{PO_4\}$ units of two symmetry-equivalent $Mn\{P_4Mo_6\}_2$ clusters, along with two oxygen atoms (O28 and $O28^1$) from two adjacent symmetry-equivalent water molecules. The bond lengths of Mn2–O27, Mn2–O28 and Mn2–O29 are 2.134(5) Å, 2.184(6) Å and 2.236(5) Å, respectively. As illustrated in Fig. 1b and S3, each $Mn\{P_4Mo_6\}_2$ cluster serves as a bridging unit between two Mn2 centers, while each Mn2 center in turn connects two neighbouring $Mn\{P_4Mo_6\}_2$ clusters, thereby assembling into a 1D inorganic chain-like structure. These parallel-aligned chains further interact with protonated $[H_2bbbm]^{2+}$ ions through some C–H···O and N–H···O hydrogen bonds, forming a 2D layered structure (Fig. 1c and Table S5). The remaining protonated $[H_2bbbm]^{2+}$ ions are situated within the interlamellar gaps, where they interact with adjacent 2D layers through multiple C–H···O and N–H···O hydrogen bonds, ultimately extending the 2D layers into a 3D supramolecular structure (Fig. 1d and S5). Functioning as both linking units and counter cations, the protonated $[H_2bbbm]^{2+}$ ions facilitate the stabilization of the integral structure of compound **1** (Fig. S4).

Meanwhile, compound **2** also was crystallized in the $P\bar{1}$ space group (Table 1). The basic structural unit of compound **2** consists of half of $\{Ni[P_4Mo_6O_{31}H_8]_2\}^{6-}$ (abbreviated as $Ni\{P_4Mo_6\}_2$) inorganic anionic cluster, 3/2 protonated $[H_2bbbm]^{2+}$ ions and six lattice water molecules (Fig. S6). The structure contains one crystallographically independent Ni1 center. The metal central Ni1 atom adopts a six-coordinated configuration, bonding to six μ_2-O atoms with twelve edge-sharing $\{MoO_6\}$ octahedra (Fig. 2a), with Ni–O bond lengths ranging from 2.105(4) Å to 2.162(5) Å (Table S4). A central $\{PO_4\}$ tetrahedron is μ_3-O-bridged to the $\{Mo_6O_{24}\}$ ring, while the other three peripheral $\{PO_4\}$ groups are symmetrically arranged around the ring to enhance the cluster's structural stability, thereby forming the $[P_4Mo_6O_{31}]^{12-}$ cluster (Fig. S7). Two $[P_4Mo_6O_{31}]^{12-}$ subunits are linked *via* one metal Ni1 atom to obtain a sandwich-type $Ni\{P_4Mo_6\}_2$ polyanion (Fig. 2b). Remarkably, the protonated $[H_2bbbm]^{2+}$ ions not only precisely balance the framework charge but also enable the self-assembly of the three-dimensional supramolecular structure, demonstrating dual functional roles (Fig. S8). As shown in Fig. 2c, the protonated $[H_2bbbm]^{2+}$ ions mediate the formation of a 1D chain architecture by establishing two hydrogen-bonding interactions [C26–H26B···O13 and C20–H20A···O20] with $Ni\{P_4Mo_6\}_2$ cluster oxygens. Furthermore, the residual protonated $[H_2bbbm]^{2+}$ ions interconnect adjacent 1D chains *via* many intermolecular hydrogen bonds, driving the generation of a 3D supramolecular structure (Fig. 2d and e).

Physical characterization

In order to characterize the compositions and structural features of compounds **1** and **2**, many measurements were performed. The results of FT-IR spectroscopy analysis indicate that the characteristic peaks of the protonated $[H_2bbbm]^{2+}$ ion $Mn\{P_4Mo_6\}_2$ cluster, and $Ni\{P_4Mo_6\}_2$ cluster are clearly observed as revealed in Fig. S9, showing excellent agreement with the literature (ref. 20, 33 and 38). The displayed characteristic absorption bands in the 500–1089 cm^{-1} region can be

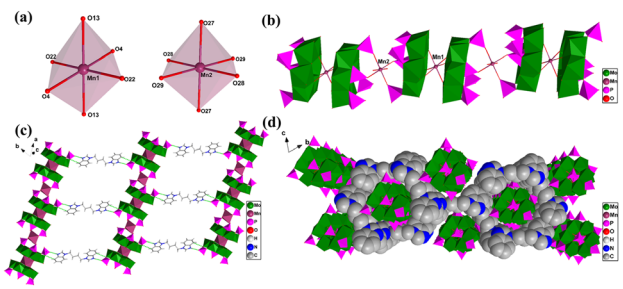

Fig. 1 (a) Coordination modes of Mn1 and Mn2 in compound **1**. (b) 1D inorganic chain constructed from $Mn\{P_4Mo_6\}_2$ clusters and Mn2 ions of compound **1**. (c) 2D supramolecular layers formed by the 1D chain through C–H···O and N–H···O hydrogen bonds of compound **1**. (d) 3D supramolecular stacking structure view showing the polyhedral inorganic sandwich-type structures and the space-filling protonated $[H_2bbbm]^{2+}$ ions of compound **1**.

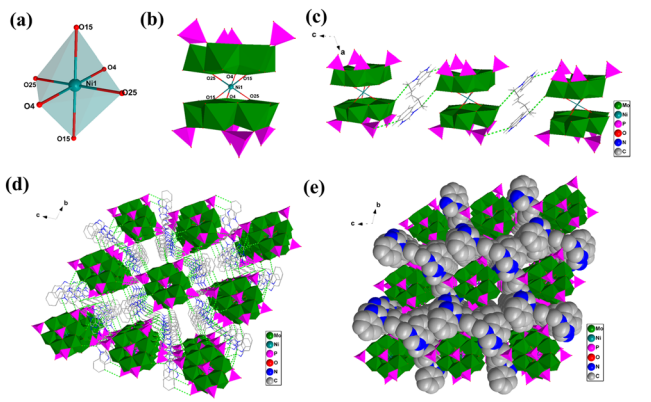

Fig. 2 (a) Coordination modes of Ni1 in compound **2**. (b) $\{Ni[P_4Mo_6O_{31}H_8]_2\}^{6-}$ cluster in compound **2**. (c) 1D chain along the *b*-axis constructed from $\{Ni[P_4Mo_6]_2\}$ polyanions and protonated $[H_2bbbm]^{2+}$ ions through hydrogen bonds in compound **1**. (d) 3D supramolecular stacking structure with a lot of C/N···O hydrogen bonds between $\{Ni[P_4Mo_6O_{31}H_8]_2\}^{6-}$ clusters and protonated $[H_2bbbm]^{2+}$ ions in compound **2**. (e) 3D supramolecular stacking structure view showing the polyhedral $\{Ni[P_4Mo_6]_2\}$ polyanions and the space-filling protonated $[H_2bbbm]^{2+}$ ions in compound **2**.

assigned to the stretching vibrations of the ν(P–O), ν(Mo–O), and ν(Mo–O–Mo) bonds within the M{P_4Mo_6}$_2$ clusters. Vibrational modes between 3200 cm^{-1} and 3574 cm^{-1} are ascribed to ν(O–H) and ν(N–H) stretching. The stretching vibrations of aromatic C–H bonds appear in the 3058–3136 cm^{-1} range. The characteristic absorption peaks in the 1260–1624 cm^{-1} region correspond to ν(C=N) stretching of benzimidazole and ν(C=C) aromatic ring stretching. The characteristic peaks at 1444 cm^{-1} for compound **1** and 1449 cm^{-1} for compound **2** correspond to ν(C=C) stretching of benzimidazole, while the characteristic peaks at 1619 cm^{-1} and 1624 cm^{-1} correspond to ν(C=C) stretching of benzimidazole.

The experimental PXRD patterns of as-synthesized compounds **1** and **2** exhibit good agreement with their simulated counterparts, with minor intensity variations, confirming their high crystallinity and phase purity (Fig. 3).

The TG curves of **1** and **2** were recorded over the temperature range of 30–1000 °C (Fig. S10). During the heating process, compound **1** underwent two stages of weight loss. The first weight-loss stage occurring in the range from 30 °C to 199 °C is due to the elimination of eight lattice water molecules with a theoretical value of 4.11% and an experimental value of 4.03%. The second stage generating weight loss between 284 °C and 915 °C is ascribed to the thermal decomposition of two water molecules coordinated with an Mn^{2+} ion, three organic $[H_2bbbm]^{2+}$ constituent ions and an Mn{P_4Mo_6}$_2$ cluster. Moreover, compound **2** similarly exhibits a two-step weight loss profile. The initial mass loss of 3.08% from 35 °C to 213 °C is attributed to the release of six lattice water molecules with a theoretical mass loss calculation of 3.12%. The second phase of mass loss is initiated at 342 °C, matching with the degradation of protonated $[H_2bbbm]^{2+}$ ions and {Ni(P_4Mo_6)$_2$} clusters. Thermogravimetric analysis revealed that both compounds maintain structural stability up to 213 °C, demonstrating remarkable thermal resistance.

To determine the composition of compounds **1** and **2** as well as the oxidation states of their constituent elements, X-ray photoelectron spectroscopy (XPS) was subsequently carried out. As shown in Fig. 4, the XPS survey spectrum confirmed the presence of Mn, O, N, C, Mo, and P on the surface of compound **1**. The Mn $2p_{1/2}$ and Mn $2p_{3/2}$ spectrum exhibited characteristic peaks at 653.8 eV and 641.6 eV, proving the Mn^{2+} oxidation state.[20] Similarly, the Mo 3d region displayed two

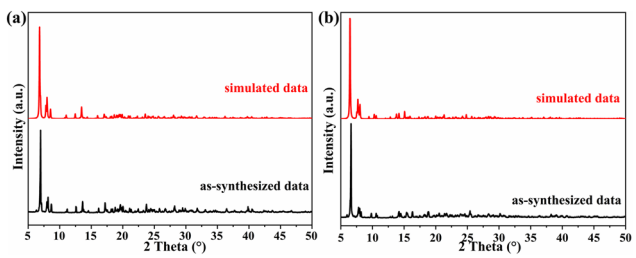

Fig. 3 (a) and (b) XRD patterns of compounds **1** and **2**, respectively.

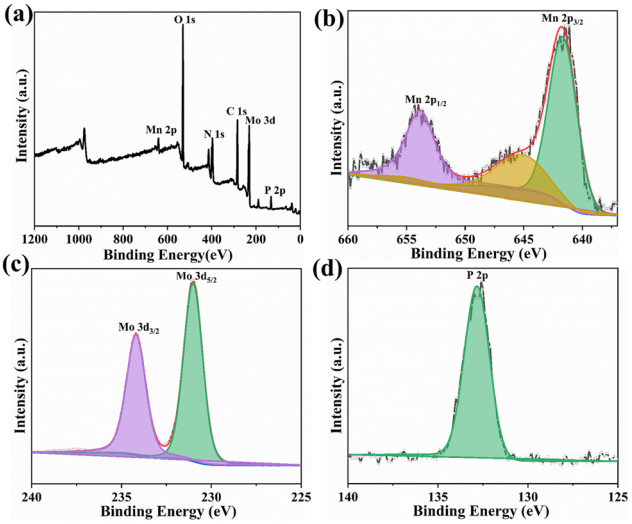

Fig. 4 (a) Overall XPS spectrum of compound **1**. (b) High-resolution XPS spectrum of Mn 2p in compound **1**. (c) High-resolution XPS spectrum of Mo 3d in compound **1**. (d) High-resolution XPS spectrum of P 2p in compound **1**.

peaks at 231.0 eV ($3d_{5/2}$) and 234.2 eV ($3d_{3/2}$), indicating the Mo^{5+} oxidation state. The characteristic peaks at 132.5 eV and 133.4 eV in the P 2p spectrum (assigned to P $2p_{3/2}$ and P $2p_{1/2}$, respectively) confirm the presence of the P^{5+} oxidation state. For compound **2**, elements Ni, O, N, C, Mo, and P were identified on its surface by XPS survey spectroscopy (Fig. S11). The Ni 2p spectrum displayed binding energies at 856.3 eV ($2p_{3/2}$) and 874.0 eV ($2p_{1/2}$), confirming the Ni^{2+} oxidation state.[38] The Mo 3d spectrum manifested peaks at 231.2 eV ($3d_{5/2}$) and 234.4 eV ($3d_{3/2}$), also corresponding to Mo^{5+}. The P 2p XPS spectrum showed two primary peaks at binding energies of 132.7 eV and 133.6 eV, corresponding to the P $2p_{3/2}$ and P $2p_{1/2}$ orbitals, respectively. This peak doublet and the associated spin–orbit splitting are characteristic of P^{5+}. These results demonstrate the consistent +5 oxidation state of Mo and P in both compounds while maintaining Mn^{2+} and Ni^{2+} states in compounds **1** and **2**, respectively. These XPS results are in good agreement with the aforementioned BVS calculations, further confirming the oxidation states of the metal centers.

Electrochemistry studies

For the purposes of evaluating the electrochemical behavior of both compounds, cyclic voltammetry (CV) measurements were performed in 0.5 M H_2SO_4 solution. The potential was swept between −0.3 and 0.6 V with scan rates varying from 30 to 150 mV s^{-1}. As shown in Fig. 5a and c, both compounds exhibit three well-defined reversible redox couples in their CV profiles, designated as I–I′, II–II′, and III–III′. As is well-known, cyclic voltammetry analysis yielded the half-wave potentials ($E_{1/2}$) through computational averaging of corresponding oxidation (E_{pa}) and reduction (E_{pc}) peaks, applying the fundamental electrochemical equation $E_{1/2} = (E_{pa} + E_{pc})/2$. Therefore, compound **1** exhibited peak potentials of $E_{1/2}$ at 0.445 V, 0.279

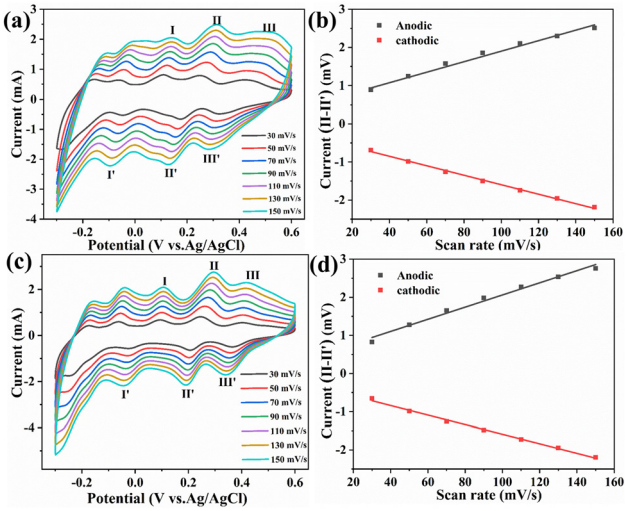

Fig. 5 (a) and (c) Cyclic voltammograms of compounds **1** and **2** at different scan rates, respectively. (b) and (d) The plots of peak current of peak (II–II′) *versus* scan rate for compounds **1** and **2**, respectively.

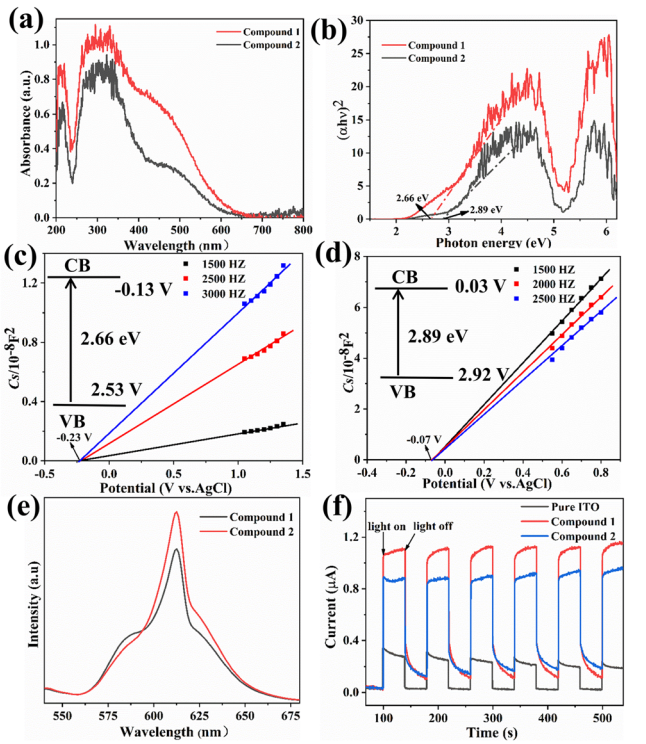

Fig. 6 (a) UV–vis DRS spectra of compounds **1** and **2**. (b) Band gap energies of compounds **1** and **2**. (c) and (d) Mott–Schottky plots and band positions of compounds **1** and **2**, respectively. (e) Fluorescence emission spectrum of compounds **1** and **2**. (f) Transient photocurrent responses of pure ITO, and compounds **1** and **2**.

V, and 0.125 V, while the corresponding values for compound **2** were 0.102 V, 0.248 V, and 0.410 V (Table S8). Furthermore, increasing the scan rate did not induce any significant shift in the positions of the three redox peaks. As illustrated in Fig. 5b and d, the peak currents of the second pair of redox peaks (II–II′) exhibited a strong linear dependence on the scan rate. These results unambiguously establish that the redox processes of both compounds are surface-dominated, showcasing exceptional electrochemical performance with highly reversible behavior.[37] Additionally, compounds **1** and **2** possess stable redox characteristics, making them promising catalysts for Cr(VI) degradation. Moreover, electrochemical impedance spectroscopy (EIS) measurements were conducted within the frequency range of 1000 to 0.01 kHz to assess the electron transfer properties of compounds **1** and **2**. The smaller charge-transfer resistance observed for compound **1** compared to compound **2** indicates enhanced electron transfer efficiency at the electrode **1** interface (Fig. S12).

UV–vis DRS and Mott–Schottky studies

The solid-state UV–vis DRS of compounds **1** and **2** were recorded to investigate their optical properties. As evidenced by the absorption spectra in Fig. 6a, both compounds exhibit a wide-range of light absorption properties encompassing both UV and visible regions (200–800 nm). While the UV region (200–400 nm) shows stronger absorption, the visible region (400–800 nm) maintains measurable absorption, enabling visible-light-driven catalysis. These spectra clearly display the characteristic features of $M\{P_4Mo_6\}_2$ clusters, consistent with literature reports.[24] This broad-spectrum photon harvesting capability in the visible region satisfies a fundamental requirement for developing high-performance reduced molybdenum phosphate photocatalysts for visible-light-driven applications. In addition, the optical band gap (E_g) values of compounds **1** and **2** were determined from Kubelka–Munk analysis of their diffuse reflectance spectra, with calculated values of 2.66 eV and 2.89 eV, respectively (Fig. 6b). All measured band gap energies fall within the optimal range for semiconductor materials, demonstrating the suitability of compounds **1** and **2** for photocatalytic applications.

Moreover, the electronic configuration of POMs demonstrates behavior similar to that of semiconductor photocatalysts, where the LUMO corresponds to the conduction band (CB), while the HOMO counterpart corresponds to the valence band (VB).[39] Analogous to semiconductor characterization, where flat band potential measurements determine CB edge positions, this method can be adapted to evaluate LUMO levels in POMs. Therefore, the positions of the CB and VB of compounds **1** and **2**, including the energy band structures, were determined using the Mott–Schottky technique. As depicted in Fig. 6c and d, compounds **1** and **2** exhibit characteristic n-type semiconductor behavior. The measured flat band potentials E_{fb} (*vs.* Ag/Ag) of compounds **1** and **2** are −0.23 V and −0.07 V, respectively. Following the established correlation for n-type semiconductors where E_{fb} is typically 0.1 V more positive than CB potentials (E_{CB}), their respective CB positions can be determined by applying the equation $E_{CB} = E_{fb} - 0.1$ V. Again, based on the equation $E_{NHE} = E_{Ag/AgCl} + 0.197$, the derived E_{CB} (*vs.* NHE) values of compounds **1** and **2**

were determined to be −0.13 V and 0.03 V, respectively. Combined with UV–vis DRS spectral analysis, the VB positions of compounds **1** and **2** were determined to be 2.53 V (*vs.* NHE) and 2.92 V (*vs.* NHE), respectively. Based on the previous results, it can be concluded that the significantly negative CB potentials of compounds **1** and **2** (−0.13 V and −0.03 V) compared to the Cr(VI)/Cr(III) redox potential (+0.51 V, pH = 7.0) provide a substantial thermodynamic driving force for Cr(VI) photoreduction. Notably, compound **1** exhibits a more negative CB position than compound **2** (−0.13 V *vs.* 0.03 V), which enhances photogenerated electron transfer efficiency and consequently improves photocatalytic Cr(VI) reduction efficiency.

Furthermore, fluorescence emission spectroscopy (Fig. 6e) revealed that compound **1** exhibited significantly lower fluorescence intensity compared to compound **2**, suggesting its enhanced ability to suppress the recombination of photogenerated electron–hole pairs, thus significantly accelerating the photocatalytic Cr(VI) reduction reaction. Moreover, to further understand the photocatalytic activities of compounds **1** and **2**, photocurrent response experiments were conducted to investigate the separation efficiency of the photogenerated electron–hole pairs. As shown in Fig. 6f, pure indium–tin oxide (ITO) glass exhibits low photo-response behavior under visible-light irradiation. In contrast, both compounds **1** and **2** generate relatively high photo-current intensities during periodic light on/off cycles. Notably, compound **1** exhibits a substantially higher photocurrent density than compound **2**, further confirming its more efficient separation of photogenerated charge carriers, which is consistent with its enhanced photocatalytic activity.

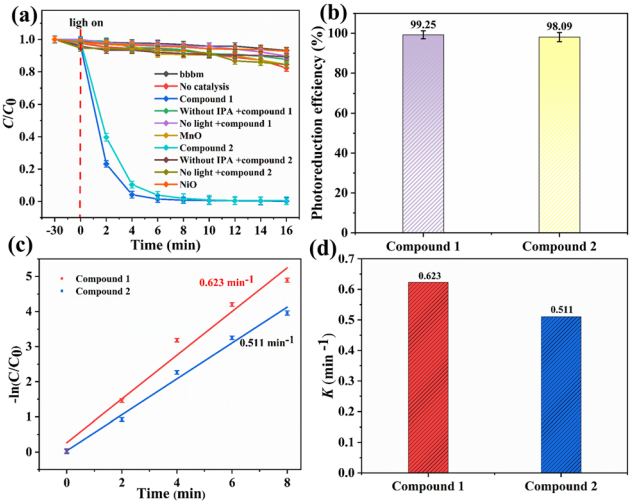

Fig. 7 (a) Profiles of the photoreduction of Cr(VI) under different controlled conditions under visible-light irradiation. (b) Performance histograms of photocatalytic Cr(VI) reduction over compounds **1** and **2**. (c) The first-order kinetics plots for the photocatalytic reduction of Cr(VI) catalysed by compounds **1** and **2**. (d) Performance histograms of the first-order kinetics plots for photocatalytic Cr(VI) reduction over compounds **1** and **2**.

Photocatalytic properties

According to previous reports, the optimal Cr(VI) reduction performance of POM-based photocatalysts typically occurs under acidic conditions (pH = 2).[15,24] Therefore, the Cr(VI) photoreduction performance of both materials was comprehensively studied in an aqueous $K_2Cr_2O_7$–IPA solution (pH = 2) under irradiation from a 300 W xenon lamp ($\lambda \geq 420$ nm). Before the reaction, the initial concentration of Cr(VI) ions in aqueous $K_2Cr_2O_7$–IPA solution was optimized. As can be observed from Fig. S14a, the process of Cr(VI) reduction is relatively rapid, and the solution quickly becomes colorless at low concentrations of 20 mg L^{-1}. As the concentration increases (40–60 mg L^{-1}), the reduction rate decreases along with the decolorization speed. Based on the comprehensive consideration of the kinetic characteristics of the Cr(VI) photocatalytic reduction reaction and the practical application requirements, 60 mg L^{-1} was chosen as the optimum working concentration. As shown in Fig. 7a and b, the Cr(VI) photoreduction efficiency exhibits significant variation across various experimental conditions. As the photocatalytic performance evaluation revealed, compounds **1** and **2** exhibited remarkable efficiency in Cr(VI) reduction when irradiated with visible light (Fig. 7a and b). Within 8 minutes, compound **1** attained a 99.25% reduction rate and compound **2** reached 98.09%. In contrast, negligible Cr(VI) reduction was observed under dark conditions, without catalyst, or when IPA was excluded, unequivocally confirming the outstanding photocatalytic efficiency of both compounds. Notably, comparative analysis with reported literature reveals that compounds **1** and **2** exhibit superior photocatalytic Cr(VI) reduction performance (Table S9). The enhanced activity may be attributed to the rigid aromatic structure of bis-benzimidazole, which can interact with organic substrates *via* π–π stacking or hydrogen bonding, thereby promoting substrate enrichment on the catalyst surface and accelerating the reaction. To elucidate the photocatalytic origin of compounds **1** and **2**, systematic control experiments were performed. Structural analysis revealed that protonated $[H_2bbbm]^{2+}$ ions serve as the protonated cationic component in both crystalline structures. Control experiments with free bbbm ligand revealed negligible photocatalytic activity, which is consistent with its weak absorption in the visible-light region (Fig. S13). This observation unambiguously confirms that the exceptional photocatalytic performance stems from the unique structural configuration of the $M\{P_4Mo_6\}_2$-based MOCs rather than from its individual components. In addition, MnO and NiO (band gap ~3.2 eV) were also evaluated as reference photocatalysts. However, negligible photocatalytic Cr(VI) reduction was observed due to their poor visible-light responses, further verifying that the $M\{P_4Mo_6\}_2$ clusters are the catalytically active species.[15] To assess the reaction dynamics, the kinetics of the photocatalytic Cr(VI) reduction was quantitatively analyzed. As shown in the Fig. 7c and d, the kinetic data demonstrated pseudo-first-order reaction behavior, as evidenced by the linear correlation in the $-\ln(C/C_0)$ *versus* time plot. The determined rate constant (k) values were 0.623 min^{-1} for compound **1** and 0.511 min^{-1} for compound **2**, indicating that the manga-

nese-based polyoxometalate exhibits faster reaction kinetics than its nickel analogue. The reported literature indicates that the catalytic activity of $\{M(P_4Mo_6)_2\}$-based-MOCs exhibits distinct structure–activity relationships: the d-electron count of metal nodes (M) governs redox potentials, the π-conjugation of organic ligands modulates charge transfer efficiency, and the geometric configuration of connection points regulates substrate accessibility.[27,40] Compound **1** exhibits superior photocatalytic activity likely due to its 1D structural architecture, which provides continuous electron transport channels that significantly reduce charge recombination.[41] To evaluate the environmental applicability, both compounds were tested for Cr(VI) reduction in real water samples including tap water and Xu Shui River water. As shown in Fig. 8a and b, the Cr(VI) reduction efficiencies in Xu Shui River water reached 97.68% and 95.80% within 8 minutes. The corresponding first-order rate constants followed the order Xu Shui River water (0.378 min^{-1}) < tap water (0.465 min^{-1}) < ultrapure water (0.623 min^{-1}). Similarly, for compound **2** the Cr(VI) reduction efficiencies in Xu Shui River water were 97.85% and 95.35% after 8 minutes, with the rate constants also following the trend: Xu Shui River water (0.391 min^{-1}) < tap water (0.484 min^{-1}) < ultrapure water (0.511 min^{-1}) (Fig. S15a and S15b). The slight decline in photocatalytic performance observed in real water sources may be attributed to competitive adsorption from common anions. Nevertheless, both compounds maintained high Cr(VI) reduction efficiency values under these conditions, demonstrating their strong potential for practical applications.

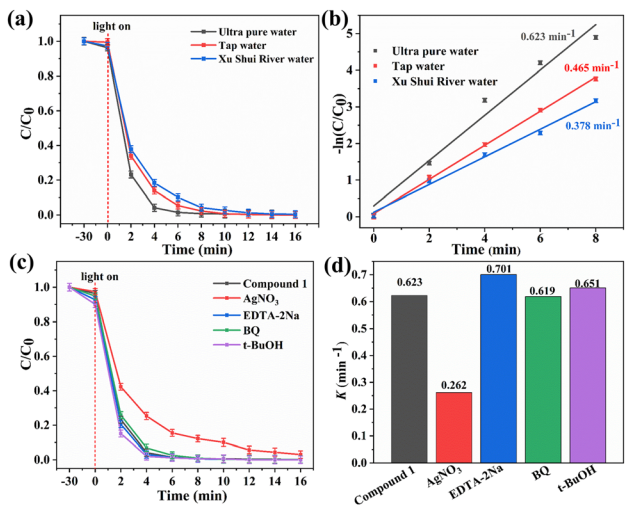

Fig. 8 (a) Profiles of the photoreduction of Cr(VI) in different water samples under visible-light irradiation by compound **1**. (b) The first-order kinetics plots for the photocatalytic reduction of Cr(VI) catalysed in different water samples under visible-light irradiation by compound **1**. (c) Profiles of the photoreduction of Cr(VI) in the presence of different scavengers for **1**. (d) Performance histograms of the first-order kinetics plots for photocatalytic Cr(VI) reduction in the presence of different scavengers by compound **1**.

To elucidate the photocatalytic mechanism of Cr(VI) removal, radical trapping experiments were performed by introducing specific scavengers into the reaction system containing compound **1** or **2**. The scavengers used were $AgNO_3$ (for electrons, e^-), EDTA-2Na (for holes, h^+), *p*-benzoquinone (BQ) (for the superoxide radical, $^{\bullet}O_2^-$), and *tert*-butanol (*t*-BuOH) (for the hydroxyl radical $^{\bullet}OH$). As shown in Fig. 8c, the addition of BQ had little influence on the photocatalytic activity of compound **1**, while EDTA-2Na and *t*-BuOH caused moderate promotion. These results indicate that during the photocatalytic reaction process, holes and hydroxyl radicals were produced, but no superoxide radicals were generated. In contrast, the photoreduction efficiency of Cr(VI) was reduced to 87.70% with the addition of $AgNO_3$. Kinetic analysis revealed that the apparent first-order rate constants followed the sequence $AgNO_3$ (0.262 min^{-1}) < BQ (0.619 min^{-1}) < compound **1** (0.623 min^{-1}) < *t*-BuOH (0.651 min^{-1}) < EDTA-2Na (0.701 min^{-1}) (Fig. 8d). Specifically, the rate constant decreased from 0.623 min^{-1} to 0.262 min^{-1} upon addition of $AgNO_3$, since $AgNO_3$ acts as a scavenger for electrons. This significant decrease indicates that photogenerated electrons are the key active species responsible for Cr(VI) reduction over compound **1**. Similarly, for compound **2**, the addition of BQ had a negligible impact on the photocatalytic activity. Conversely, the addition of EDTA-2Na and *t*-BuOH resulted in a partial enhancement of the activity, whereas the introduction of $AgNO_3$ significantly inhibited the reaction, reducing the Cr(VI) reduction efficiency to 89.90% (Fig. S15c). These results also indicate that during the photocatalytic process, h^+, $^{\bullet}OH$, and e^- were generated, whereas no $^{\bullet}O_2^-$ was detected. As shown in Fig. S15d, the corresponding rate constants obeyed the following order: $AgNO_3$ (0.280 min^{-1}) < BQ (0.493 min^{-1}) < compound **2** (0.511 min^{-1}) < EDTA-2Na (0.641 min^{-1}) < *t*-BuOH (0.706 min^{-1}). The rate constant also decreased from 0.511 min^{-1} to 0.280 min^{-1} with the addition of $AgNO_3$. This consistent behavior further confirms that photogenerated electrons (e^-) serve as the primary active species responsible for the reduction of Cr(VI) for both compounds.

Based on the above results, the possible mechanisms of photocatalytic Cr(VI) reduction for both compounds are proposed (Fig. 9, S16 and Scheme 2). Under visible-light

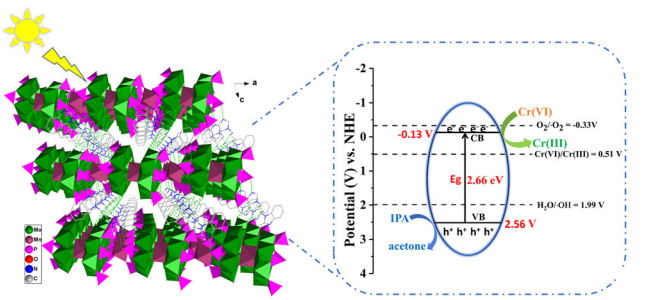

Fig. 9 Possible photocatalytic reaction mechanism of the photoreduction of Cr(VI) catalyzed by compound **1** under visible-light irradiation.

$$POM \xrightarrow{\text{Irradiation}} POM(e^- - h^+) \quad (1)$$

$$IPA + h^+ \longrightarrow CH_3COCH_3 + H^+ \quad (2)$$

$$H_2O + h^+ \longrightarrow \cdot OH^- + H^+ \quad (3)$$

$$IPA + \cdot OH^- \longrightarrow CH_3COCH_3 + H_2O \quad (4)$$

$$Cr_2O_7^{2-} + 6e^- + 14H^+ \longrightarrow 2Cr^{3+} + 7H_2O \quad (5)$$

Scheme 2 The possible photocatalytic oxidation–reduction reactions over compounds **1** and **2** acting as photocatalysts in this paper.

irradiation, compounds **1** and **2** function as photocatalysts and are excited to produce photoelectron (e^-) and photogenerated hole (h^+) pairs. Then, the photoelectrons (e^-) immediately facilitated the reduction of toxic Cr(VI) to the less hazardous Cr (III). The conduction bands of compounds **1** and **2** are −0.13 V *vs.* NHE and 0.03 V *vs.* NHE more negative than that of Cr(VI)/Cr(III) (0.51 V *vs.* NHE), respectively. Subsequently, photogenerated holes (h^+) are scavenged by isopropanol, which undergoes oxidation to acetone. Because the E_{VB} values of compound **1** (+2.53 eV) and compound **2** (+2.92 eV) are higher than the standard redox potentials of $H_2O/^{\bullet}OH^-$ (+1.99 eV *vs.* NHE), some hydroxyl radicals may be generated. The isopropanol can also be oxidized by the hydroxyl radicals to produce acetone and H_2O. This dual process accelerates charge carrier separation efficiency and consequently improves photocatalytic performance. The possible reaction equations for the whole photocatalytic process are shown in Scheme 2.

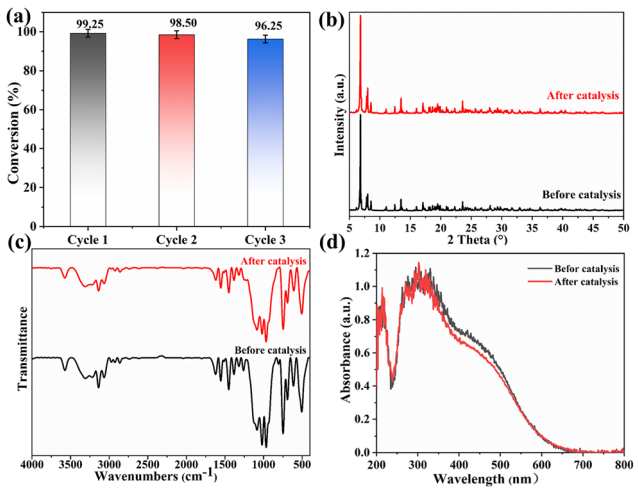

Fig. 10 (a) Recycling experiments for the photo-reduction of Cr(VI) by compound **2**. (b) XRD patterns of compound **1** before and after photocatalytic experiments. (c) FT-IR spectra of compound **1** before and after photocatalytic experiments. (d) UV–vis absorption spectra of compound **1** before and after photocatalytic experiments.

The stability and recyclability of photocatalysts represent critical parameters for practical applications, as they directly determine long-term viability and cost-effectiveness. Both compounds maintain highly efficient photocatalytic performance toward Cr(VI) reduction over three consecutive cycles, with reduction efficiencies remaining above 96.25% for compound **1** and 94.20% for compound **2** (Fig. 10a and S17a). The observed marginal decline in photocatalytic performance may be ascribed to minimal catalyst loss during the recovery process. Furthermore, the XRD, IR and UV–vis absorption spectra of both compounds after catalysis were also recorded (Fig. 10(b–d) and S17(b–d)). Comparing the results with those recorded before testing, it was shown that both compounds exhibited remarkable structural robustness and maintain excellent broadband light absorption capabilities throughout the photocatalytic process. These comprehensive spectroscopic results unambiguously demonstrate the exceptional structural integrity and photochemical stability of both compounds during prolonged photocatalytic operation.

Conclusions

In conclusion, two reduced phosphomolybdate-based MOCs, **1** and **2**, were successfully synthesized *via* hydrothermal methods using a flexible bis(1*H*-benzimidazole) bbbm ligand. These compounds feature a unique 1D + 0D → 3D supramolecular architecture. Both compounds exhibit broad visible-light absorption and optimal band structures, enabling exceptional photocatalytic Cr(VI) reduction with rapid removal rates of 99.25% for compound **1** and 98.09% for compound **2** within 8 minutes under visible-light irradiation. The reaction follows pseudo-first-order kinetics, with rate constant (k) values of 0.623 min^{-1} for compound **1** and 0.511 min^{-1} for compound **2**. These results clearly demonstrate the superior catalytic performance of compound **1** over that of compound **2**. Notably, the materials maintain high efficiency and stability even in real water samples. Mechanistic studies demonstrate that $M\{P_4Mo_6\}_2$ clusters play a critical role in photocatalytic performance, with enhanced activity arising from synergistic interactions between reduced phosphomolybdate units and the organic ligand bbbm. This study not only offers molecular-level design tactics for high-performance $M\{P_4Mo_6\}_2$-based photocatalysts but also highlights the importance of structural dimensionality in optimizing photocatalytic performance. These findings offer valuable insights into structure–activity relationships and pave the way for future developments in environmental photocatalysis. Our future studies will focus on: (1) optimizing the tunability of ligands to further enhance photocatalytic efficiency through targeted structural modifications, and (2) expansion of the material's application to other environmentally relevant heavy metal pollutants. These investigations will not only advance the fundamental understanding of phosphomolybdate-based photocatalysis but also promote practical applications in environmental remediation.

Author contributions

Feng-Cai Li: conceptualization, validation and writing. Xi-Li Li, Yu-Zhe Pan, Cong-Li Gao, and Qing-Xiang Yang: investigation, review & editing and supervision. Feng-Cai Li: conceptualization, supervision and funding acquisition.

Conflicts of interest

There are no conflicts to declare.

Data availability

All relevant data are within the manuscript and its SI. Supplementary information: Experimental section, supplementary figures (*e.g.*, structural figures, IR spectra, TG curves, and EIS spectra), and supplementary tables (*e.g.*, selected bond lengths/angles, hydrogen bonding parameters, and bond valence sum results). See DOI: **https://doi.org/10.1039/d5dt01698c**.

CCDC 2449146 and 2449148 contain the supplementary crystallographic data for this paper.[42a,b]

Acknowledgements

The authors acknowledge the financial support of the National Natural Science Foundation of China (No. 21501151), the Science and Technology Research Project in Henan Province (232102230032), and the Key Scientific Research Project of Higher Education Institutions in Henan Province (25A150022).

References

1 H. Zhao, Z. Xing, S. Su, S. Song, T. Xu, Z. Li and W. Zhou, *Appl. Mater. Today*, 2020, **21**, 100821–100835.
2 L. A. Malik, A. Bashir, A. Qureashi and A. H. Pandith, *Environ. Chem. Lett.*, 2019, **17**, 1495–1521.
3 W. I. Mortada, A. El-Naggar, A. Mosa, K. N. Palansooriya, B. Yousaf, R. Tang, S. Wang, Y. Cai and S. X. Chang, *Chemosphere*, 2023, **331**, 138804.
4 Y. Fang, J. Wen, H. Zhang, Q. Wang and X. Hu, *Environ. Pollut.*, 2020, **260**, 114021.
5 S. M. Ghoreishian, K. S. Ranjith, B. Park, S. K. Hwang, R. Hosseini, R. Behjatmanesh-Ardakani, S. M. Pourmortazavi, H. U. Lee, B. Son, S. Mirsadeghi, Y. K. Han and Y. S. Huh, *Chem. Eng. J.*, 2021, **419**, 129530.
6 A. K. Mallik, M. A. Moktadir, M. A. Rahman, M. Shahruzzaman and M. M. Rahman, *J. Hazard. Mater.*, 2022, **423**, 127041.
7 K. E. Ukhurebor, U. O. Aigbe, R. B. Onyancha, W. Nwankwo, O. A. Osibote, H. K. Paumo, O. M. Ama, C. O. Adetunji and I. U. Siloko, *J. Environ. Manag.*, 2021, **280**, 111809–111833.
8 S. M. Ghoreishian, K. S. Ranjith, M. Ghasemi, B. Park, S.-K. Hwang, N. Irannejad, M. Norouzi, S. Y. Park, R. Behjatmanesh-Ardakani, S. M. Pourmortazavi, S. Mirsadeghi, Y.-K. Han and Y. S. Huh, *Chem. Eng. J.*, 2023, **452**, 139435.
9 M. Jafarzadeh, *ACS Appl. Mater. Interfaces*, 2022, **14**, 24993–25024.
10 S. Ye, Y. Chen, X. Yao and J. Zhang, *Chemosphere*, 2021, **273**, 128503–128514.
11 B. Wang and R. Wang, *J. Hazard. Mater.*, 2025, **495**, 139037.
12 X. Y. Ma, H. X. Bi, X. J. Zhang, J. Du, Y. Y. Ma and Z. G. Han, *Polyoxometalates*, 2025, **4**, 9140090.
13 J. Y. He, J. F. Wang, J. Du, Y. Y. Ma and Z. G. Han, *Eur. J. Inorg. Chem.*, 2025, **28**, e202400584.
14 Y. Q. Zhang, L. Y. Zhou, Y. Y. Ma, K. Dastafkan, C. Zhao, L. Z. Wang and Z. G. Han, *Chem. Sci.*, 2021, **12**, 1886–1890.
15 H. X. Bi, L. Hou, X. Y. Yin, Y. Y. Ma and Z. G. Han, *Cryst. Growth Des.*, 2022, **22**, 738–746.
16 W. Deng, Z. Zhu, Y. Sun, H. Xu, S. Liu and H. Wen, *Polyoxometalates*, 2024, **3**, 9140071.
17 H. X. Bi, M. S. Guo, J. Du, Y. Y. Ma and Z. G. Han, *Coord. Chem. Rev.*, 2024, **518**, 216092.
18 J. F. Wang, C. X. Yin, J. X. Qi, Y. Y. Ma, Z. G. Lin and Z. G. Han, *Chem. Commun.*, 2025, **61**, 1914–1917.
19 M. S. Guo, C. X. Yin, Z. Y. Zhang, Y. Y. Ma, J. Du and Z. G. Han, *Chin. Chem. Lett.*, 2025, 111158.
20 Y. J. Li, C. X. Li, S. B. Zhou, J. Y. Wei, Q. Fang, X. L. Hu, B. L. Liu and Z. M. Su, *Inorg. Chem.*, 2025, **64**, 443–451.
21 X. Wang, X. Liu, N. Xu, X. Liu, Y. Guo, X. Zhang and X. Li, *Inorg. Chem.*, 2023, **62**, 12181–12186.
22 J. S. Yeon, W. I. Kim, H. J. Kim, G. Jang, J. M. Park, J. H. Park, Y. Li and H. S. Park, *Energy Storage Mater.*, 2023, **63**, 102944.
23 Z. X. Gao, S. Sun, B. Li, D. M. Cheng, Y. H. Wang, H. Y. Zang and Y.-G. Li, *Tungsten*, 2023, **5**, 67–74.
24 X. Y. Yin, H. X. Bi, H. Song, J. Y. He, Y. Y. Ma, T. T. Fang and Z.-G. Han, *Polyoxometalates*, 2023, **2**, 9140027–9140038.
25 C. Geng, J. Niu, D. Zhao, X. Jin, J. Liu, X. Liu and D. K. Y. Wong, *Chem. Eng. J.*, 2023, **475**, 146302.
26 X. Xin, X. Tian, H. Yu and Z. Han, *Inorg. Chem.*, 2018, **57**, 11474–11481.
27 J. Y. He, H. X. Bi, Y. Q. Liu, M. S. Guo, W. T. An, Y. Y. Ma and Z. G. Han, *Inorg. Chem.*, 2024, **63**, 842–851.
28 W. An, X. Zhang, J. Niu, Y. Ma and Z. Han, *Chin. Chem. Lett.*, 2022, **33**, 4400–4404.
29 Y. Benseghir, A. Solé-Daura, P. Mialane, J. Marrot, L. Dalecky, S. Béchu, M. Frégnaux, M. Gomez-Mingot, M. Fontecave, C. Mellot-Draznieks and A. Dolbecq, *ACS Catal.*, 2022, **12**, 453–464.
30 J.-P. Cao, Y. Ren, H. Ding, J. Shang, B. Yue and H. He, *Inorg. Chem. Commun.*, 2023, **155**, 111053.
31 Y. Q. Zhang, L. Hou, H. X. Bi, X. X. Fang, Y. Y. Ma and Z. G. Han, *Chem. – Asian J.*, 2021, **16**, 1584–1591.
32 S. Y. Hao, S. X. Hou, K. Van Hecke and G. H. Cui, *Dalton Trans.*, 2017, **46**, 1951–1964.

33 S. Liu, Y. Yang, Y. Qi, X. Meng and H. Hou, *J. Mol. Struct.*, 2010, **975**, 154–159.
34 X. Wang, W. Mao, D. Wang, X. Hu, B. Liu and Z. Su, *Talanta*, 2023, **257**, 124270.
35 B. Xiao, H. Han, X. Meng, Y. Song, Y. Fan, H. Hou and Y. Zhu, *Inorg. Chem. Commun.*, 2004, **7**, 378–381.
36 O. V. Dolomanov, L. J. Bourhis, R. J. Gildea, J. A. K. Howard and H. Puschmann, *J. Appl. Crystallogr.*, 2009, **42**, 339–341.
37 X. H. Liu, L. B. Zhang, J. L. Wang, N. Xu, X. Y. Zhang, Z. H. Chang and X. L. Wang, *Inorg. Chem.*, 2024, **63**, 9058–9065.
38 Y. Li, N. Zhu, Z. Su, X. Hu, Z. Dou and Z. Su, *Inorg. Chem. Front.*, 2024, **11**, 2598–2607.
39 Q. Cen, Q. Gao, C. Zhang, Y. Liu, Q. Wang and Q. Wang, *J. Colloid Interface Sci.*, 2020, **562**, 12–20.
40 H. X. Bi, X. Y. Yin, J. Y. He, H. Song, S. J. Lu, Y. Y. Ma and Z. G. Han, *Rare Met.*, 2023, **42**, 3638–3650.
41 L. Hou, Y. Zhang, Y. Ma, Y. Wang, Z. Hu, Y. Gao and Z. Han, *Inorg. Chem.*, 2019, **58**, 16667–16675.
42 (*a*) F.-C. Li, X.-L. Li, Y.-Z. Pan, C.-L. Gao and Q.-X. Yang, CCDC 2449146: Experimental Crystal Structure Determination, 2025, DOI: **10.5517/ccdc.csd.cc2n6jq4**; (*b*) F.-C. Li, X.-L. Li, Y.-Z. Pan, C.-L. Gao and Q.-X. Yang, CCDC 2449148: Experimental Crystal Structure Determination, 2025, DOI: **10.5517/ccdc.csd.cc2n6js6**.